Autonomous stabilization with programmable stabilized states

SUPPLEMENTARY NOTE 1: DEVICE HAMILTONIAN AND REALIZED SIDEBANDS

Supplementary Figure 1 shows the inductively coupled two-qubit device used in the stabilization demonstration. Two transmon qubits (red) share a common ground, which is interrupted by a SQUID (purple). Each transmon is capacitively coupled to a lossy resonator (green) also serving as the dispersive readout. In our stabilization protocol, two types of sideband interactions are necessary: Qubit-Qubit sidebands (QQ) and Qubit-Resonator (QR) sidebands. We will theoretically show how these interactions are engineered from the system's Hamiltonian and provide the corresponding interaction strength.

A. QQ sideband

The flux line near the SQUID provides a continuous DC bias $\varphi_{\rm dc} = 0.3795\pi$ in our experiment. The measured qubit coherence and frequencies at this flux point are shown in Supplementary Table 1. By sending RF flux drives at appropriate frequencies through the flux line, the inductive coupler can provide either QQ red sideband or QQ blue sideband. The Hamiltonian for qubits and coupler is shown in Supplementary Eq. 1a. For a detailed description on the adiabatic approximation of the inductive coupler, we draw the attention of the readers to the references 1 and 2. Following is a summary. The Hamiltonian of the circuit containing two qubits and the coupler is described by

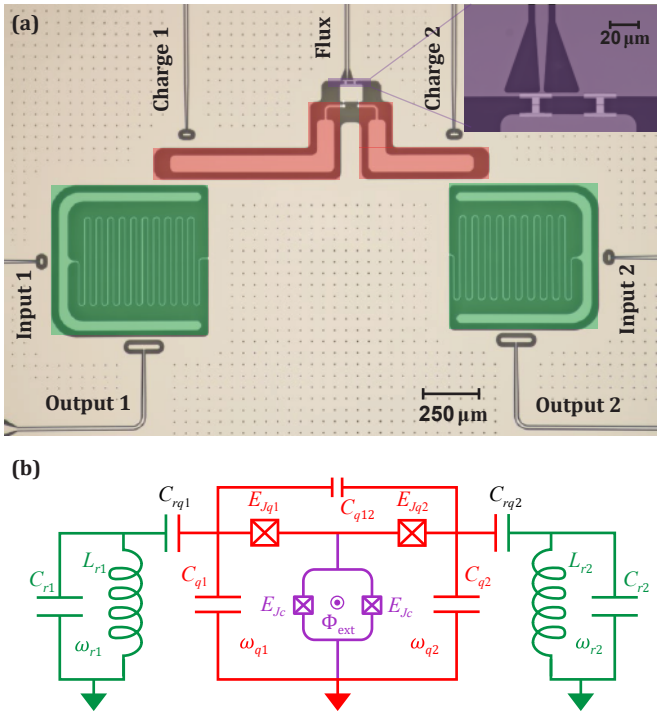

Supplementary Figure 1. The device. (a) False-colored optical image of the device. The inset shows a zoomed-in image of the inductive coupler. (b) Circuit diagram of the device. Coupler junctions' intrinsic capacitance C_{qc} is included in the quantization analysis.

$\varphi_{\rm dc} = 0.0$	$T_1(\mu s)$	$T_{\rm Ram}(\mu s)$	$T_{\rm echo}(\mu s)$
Q_1	31.6	28.4	26.6
Q_2	2.8	4.9	

$\varphi_{\rm dc} = 0.3795\pi$	$T_1(\mu s)$	$T_{\rm Ram}(\mu s)$	$T_{\rm echo}(\mu s)$
Q_1	24.3	15.2	24.6
Q_2	9.1	9.8	14.3
R_1	0.48		
R_2	0.37		

Parameter	Symbol	Value/2π
Q_1 ge frequency	$\omega_{q1}/2\pi$	3.2046 (GHz)
Q_2 ge frequency	$\omega_{q2}/2\pi$	3.6624 (GHz)
Q_1 anharmonicity	$\alpha_1/2\pi$	−116.3 (MHz)
Q_2 anharmonicity	$\alpha_2/2\pi$	−159.5 (MHz)
Readout1 frequency	$\omega_{r1}/2\pi$	4.9946 (GHz)
Readout2 frequency	$\omega_{r2}/2\pi$	5.4505 (GHz)
$(E_{\lvert ee\rangle} - E_{\lvert ge\rangle}) - (E_{\lvert eg\rangle} - E_{\lvert gg\rangle})$	$ZZ/2\pi$	-261 (kHz)
Readout1 fidelity		88.87%
Readout2 fidelity		81.76%

Supplementary Table 1. Device coherence and frequencies at the coupler biasing point $\varphi_{\rm dc} = 0.3795\pi$ (top and middle), and the coherence at the coupler sweet spot $\Phi_{\rm dc} = 0\pi$ (bottom). Q_2 experiences higher loss at the sweet spot from a near two-level system. At the sweet spot, Q_1's decoherence and echo time are similar to those at our experiment's biasing point.

$$H = \vec{n}^{\intercal} C_L^{-1} \vec{n} - E_{j1}\cos(\phi_c - \phi_1) - E_{j2}\cos(\phi_2 - \phi_c), \\ - E_{jc}\cos\left(\frac{\Phi_{\rm ext}}{\Phi_0}\right)\cos(\phi_c), \tag{1a}$$

$$C_L = \begin{bmatrix} C_{q1} + C_{q12} & -C_{q12} & 0 \\ -C_{q12} & C_{q2} + C_{q12} & 0 \\ 0 & 0 & C_{q1} + C_{q2} + C_{qc} \end{bmatrix} \tag{1b}$$

$$\vec{n}^{\intercal} = (n_1, n_2, n_c)\,.$$

Here, phase variables $\phi_{1,2,c}$, charge variables $n_{1,2,c}$, and Josephson energy $E_{j1,j2,jc}$ are for qubit 1, qubit 2, and the coupler, and C_{qc} is the intrinsic capacitance from the coupler junction. After quantization, one can arrive at

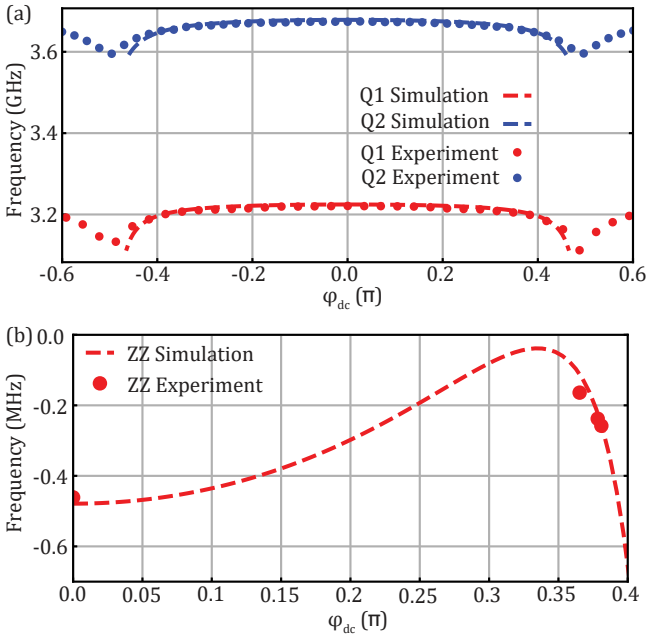

Supplementary Figure 2. Coupler DC flux sweep of (a) qubits frequencies and (b) ZZ coupling strength between qubits. Circuit quantization results and experimentally measured data are separately shown in dash lines and dots.

the following:

$$\begin{aligned} H_{ab} =&\omega_{q1} a_{q1}^{\dagger} a_{q1} + \omega_{q2} a_{q2}^{\dagger} a_{q2} \\ &+ \frac{\alpha_1}{2} a_{q1}^{\dagger} a_{q1}^{\dagger} a_{q1} a_{q1} + \frac{\alpha_2}{2} a_{q2}^{\dagger} a_{q2}^{\dagger} a_{q2} a_{q2} \\ &+ g_1(t) \left(a_{q1}^{\dagger} + a_{q1}\right)\left(a_{q2}^{\dagger} + a_{q2}\right) \\ &+ g_2 \left(-a_{q1}^{\dagger} + a_{q1}\right)\left(-a_{q2}^{\dagger} + a_{q2}\right), \end{aligned} \tag{2a}$$

$$g_1(t) = \frac{\sqrt{E_{j1} E_{j2}}}{2E_{jc} \cos\left(\frac{\Phi_{\text{ext}}(t)}{\Phi_0}\right)} \sqrt{\omega_{q1}\omega_{q2}}, \tag{2b}$$

$$g_2 = \frac{\sqrt{C_{q1} C_{q2}}}{2C_{q12}} \sqrt{\omega_{q1}\omega_{q2}}. \tag{2c}$$

In the experiment, we have $E_{jc} = 1700\,\text{GHz} \gg E_{j1}(E_{j2}) = 12.2\,\text{GHz}(12.3\,\text{GHz})$, making the coupler mode much heavier than the qubit modes. This strong asymmetry enables the adiabatic removal of the coupler dynamics: We treat the coupler as a linear inductance and assume the coupler mode is static. By removing the linear mode through minimizing the system energy, we arrive at the approximated Hamiltonian in Supplementary Eq. 2a. When modulating the external RF flux threaded the coupler, the transverse coupling strength $g_1(t)$ will also be modulated accordingly. By plugging the RF flux modulation $\Phi_{\text{ext}}/\Phi_0 = \varphi_{\text{dc}} + \epsilon\cos(\omega_d t)$ into Supplementary Eq. 2b and assuming the flux modulation ϵ is much smaller than Φ_{dc}, we have:

$$\begin{aligned} g_1(t) =& \frac{\sqrt{E_{j1} E_{j2}}}{2E_{jc}} \sqrt{\omega_{q1}\omega_{q2}} \frac{1}{\cos\left(\varphi_{\text{dc}} + \epsilon\cos(\omega_d t)\right)} \\ \approx& \frac{\sqrt{E_{j1} E_{j2}}}{2E_{jc}} \sqrt{\omega_{q1}\omega_{q2}} \frac{\left(1 + \epsilon\sin(\omega_d t)\tan(\varphi_{\text{dc}})\right)}{\cos(\varphi_{\text{dc}})} \end{aligned} \tag{3a}$$

Under the rotating frame transformation $U = e^{1j\omega_{q1} a_{q1}^{\dagger} a_{q1} t} e^{1j\omega_{q2} a_{q2}^{\dagger} a_{q2} t}$, we have:

$$\begin{aligned} \tilde{H}_{ab} =& U H_{ab} U^{\dagger} \\ =& \frac{\alpha_1}{2} a_{q1}^{\dagger} a_{q1}^{\dagger} a_{q1} a_{q1} + \frac{\alpha_2}{2} a_{q2}^{\dagger} a_{q2}^{\dagger} a_{q2} a_{q2} \\ &+ g_1(t) \left(a_{q1}^{\dagger} e^{1j\omega_{q1} t} + a_{q1} e^{-1j\omega_{q1} t}\right) \\ &\times \left(a_{q2}^{\dagger} e^{1j\omega_{q2} t} + a_{q2} e^{-1j\omega_{q2} t}\right) \\ &+ g_2 \left(-a_{q1}^{\dagger} e^{1j\omega_{q1} t} + a_{q1} e^{-1j\omega_{q1} t}\right) \\ &\times \left(-a_{q2}^{\dagger} e^{1j\omega_{q2} t} + a_{q2} e^{-1j\omega_{q2} t}\right) \end{aligned} \tag{4a}$$

We then assume the transmon anharmonicity α_i is much larger than the sideband strength. Each transmon Hamiltonian can be projected to a two-level system and neglect the population in the higher level:

$$\begin{aligned} \tilde{H}_{TLS} =& g_1(t) \left(a_{q1}^{\dagger} e^{1j\omega_{q1} t} + a_{q1} e^{-1j\omega_{q1} t}\right) \\ &\times \left(a_{q2}^{\dagger} e^{1j\omega_{q2} t} + a_{q2} e^{-1j\omega_{q2} t}\right) \\ &+ g_2 \left(-a_{q1}^{\dagger} e^{1j\omega_{q1} t} + a_{q1} e^{-1j\omega_{q1} t}\right) \\ &\times \left(-a_{q2}^{\dagger} e^{1j\omega_{q2} t} + a_{q2} e^{-1j\omega_{q2} t}\right) \end{aligned} \tag{5a}$$

By choosing the modulation frequency $\omega_d = \omega_{q1} \pm \omega_{q2}$, plug in the form of $g_1(t)$ and keep only static term and neglect fast rotating term (Rotating Wave Approximation), we have:

$$\tilde{H}_{red} = \epsilon \frac{\sqrt{E_{j1} E_{j2}}}{2E_{jc}} \sqrt{\omega_{q1}\omega_{q2}} \frac{\tan(\varphi_{\text{dc}})}{2\cos(\varphi_{\text{dc}})}(t)\, a_{q1}^{\dagger} a_{q2} + h.c. \tag{6a}$$

$$\tilde{H}_{blue} = \epsilon \frac{\sqrt{E_{j1} E_{j2}}}{2E_{jc}} \sqrt{\omega_{q1}\omega_{q2}} \frac{\tan(\varphi_{\text{dc}})}{2\cos(\varphi_{\text{dc}})}(t)\, a_{q1} a_{q2} + h.c. \tag{6b}$$

Here, H_{red} and H_{blue} are separately the red and blue sideband interactions between two transmons (restricted to the first two levels). Therefore the QQ sideband rate is:

$$\epsilon \frac{\sqrt{E_{j1} E_{j2}}}{2E_{jc}} \sqrt{\omega_{q1}\omega_{q2}} \frac{\tan(\varphi_{\text{dc}})}{\cos(\varphi_{\text{dc}})} \tag{7}$$

Here, the factor of 2 difference comes from the convention to define the rate at the lab frame. The sideband rate is proportional to the flux modulation rate and increases with $\varphi_{\rm dc}$. We choose $\varphi_{\rm dc} = 0.3795\pi$ based on qubit coherence, sideband rate, and small ZZ coupling between qubits.

B. QR sideband

The QR sideband can also be realized through flux modulation. When the resonator is capacitively coupled to the qubit at strength g_{qri} and frequency difference $\Delta_i = \omega_{qi} - \omega_{ri}$, the transmon level is dressed by the resonator:

$$a'_{qi} = a_{qi} + \frac{g_{qri}}{\Delta_i} a_{ri} \tag{8}$$

Here a'_{qi} is the transmon annihilation operator in the dressed basis. Replacing a_{qi} with a'_{qi} in $\tilde{H}_{TLS}$, and choose $\omega_d = \omega_{ri} \pm \omega_{qi}$, we can active QR red and blue sideband between Q_1R_1 and between Q_2R_2. The QR sideband rate through flux modulation is:

$$\epsilon \frac{g_{qri}}{\Delta_i} \frac{\sqrt{E_{j1}E_{j2}}}{2E_{jc}} \sqrt{\omega_{q1}\omega_{q2}} \frac{\tan(\varphi_{\rm dc})}{\cos(\varphi_{\rm dc})}. \tag{9}$$

In our system, the QR blue sideband frequencies are beyond the hardware limit (> 8GHz). Therefore, we choose only to activate the QR red sideband through the flux line.

The QR blue sidebands have a different choice to activate [3]: The direct charge drives at half of the transition frequency with amplitude ϵ_q can provide an effective QR blue sideband rate:

$$16 g_{qri}^3 \epsilon_q^2 / \Delta_i^4. \tag{10}$$

This turned out to be easier to realize with our device, and we achieve at least 0.5 MHz QR blue sideband rate.

C. Experimental data

Supplementary Figure 3 demonstrates all realized QQ and QR sidebands needed for the stabilization experiments. Fast QQ red sidebands at 8.5 MHz and modest QQ blue sidebands at 3.9 MHz are performed in the experiment through RF flux modulation of the inductive coupler. Both readouts for QQ red sideband (with initial state $|eg\rangle$) and QQ blue sideband (with initial state $|gg\rangle$) are shown in Supplementary Figure 3(a) and (b). The QR blue sidebands are generated through the charge lines that are coupled to the qubit pads, shown in Supplementary Figure 3(c) with initial state $|g0\rangle$. The QR1 red sidebands are activated through the coupler flux modulation. The on-resonance readout trace for Q_1 starting at $|e0\rangle$ is plotted in Supplementary Figure 3(d).

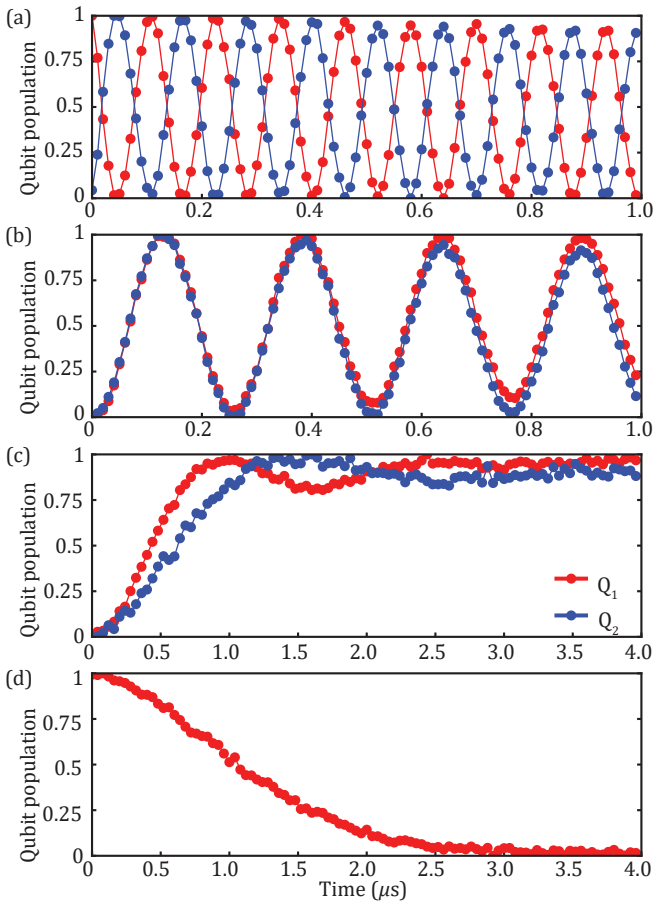

Supplementary Figure 3. Experimentally realized QQ and QR sidebands. From top to bottom are separately (a) QQ red sideband $|ge\rangle \leftrightarrow |eg\rangle$, (b) QQ blue sideband $|gg\rangle \leftrightarrow |ee\rangle$, (c) QR blue sideband between QR1 and QR2 $|g0\rangle \leftrightarrow |e1\rangle$, and (d) QR1 red sideband $|e0\rangle \leftrightarrow |g1\rangle$. Readout on Q_1 (red) and Q_2 (blue) are scaled between 0 ($|g\rangle$) and 1 ($|e\rangle$). Data points are connected for visual guidance.

In our experiments, the actual modulation frequencies of the sidebands deviate slightly from their theoretically predicted values due to the AC Stark shift. To address this, the modulation frequencies for both the QQ and QR sidebands are recalibrated. This recalibration involves optimizing the stabilization fidelity by adjusting the frequencies while all drives are on.

SUPPLEMENTARY NOTE 2: DERIVATION OF STEADY-STATE FIDELITY

We take the stabilization of $|\Psi_\theta\rangle = \sin(\theta/2)|gg\rangle - \cos(\theta/2)|ee\rangle$ as an example to compute the steady-state fidelity in detail. Suppose the steady state population at the four basis states $\{|\Psi_\theta\rangle, |ge\rangle, |eg\rangle, |\Psi_{\theta-\pi}\rangle\}$ are separately $\{w, x, y, z\}$. We assume the photon population in both resonators are transitional and ignore their contribution to the steady-state fidelity. This means

$w+x+y+z=1$. The steady-state configuration should balance the following two processes:

(a) two-step refilling process: $|ge\rangle \to |\Psi_\theta\rangle$, $|eg\rangle \to |\Psi_\theta\rangle$, $|ge\rangle \to |\Psi_\theta\rangle$, and $|ge\rangle \to |\Psi_\theta\rangle$. All the transition rates are the same

$$\Gamma_t = \frac{W^2\cos^2(\theta/2)\,\kappa}{\kappa^2 + W^2\cos^2(\theta/2)} \tag{11}$$

(b) Single photon loss in each qubit. The following four transitions have the same rate $\sin^2(\theta/2)\,\gamma$: $|ge\rangle \to |\Psi_\theta\rangle$, $|eg\rangle \to |\Psi_\theta\rangle$, $|ge\rangle \to |\Psi_{\theta-\pi}\rangle$, and $|eg\rangle \to |\Psi_{\theta-\pi}\rangle$. The reversed four transitions have the same rate $\cos^2(\theta/2)\,\gamma$.

Therefore, the steady-state population should satisfy the following equations

$$\begin{cases} \left(\Gamma_t + \sin^2(\theta/2)\,\gamma\right)(x+y) - 2\cos^2(\theta/2)\,\gamma w &= 0, \\ \left(\Gamma_t + \sin^2(\theta/2)\,\gamma\right) z + \cos^2(\theta/2)\,\gamma w - (\Gamma_t+\gamma)x &= 0, \\ \left(\Gamma_t + \sin^2(\theta/2)\,\gamma\right) z + \cos^2(\theta/2)\,\gamma w - (\Gamma_t+\gamma)y &= 0, \\ 2\cos^2(\theta/2)\,\gamma(x+y) - \left(2\Gamma_t + 2\sin^2(\theta/2)\,\gamma\right) z &= 0, \\ w+x+y+z &= 1. \end{cases} \tag{12}$$

This gives the following populations

$$\begin{cases} w &= \left(\frac{\Gamma_t+\gamma\sin^2(\theta/2)}{\Gamma_t+\gamma}\right)^2, \\ x &= \frac{\cos^2(\theta/2)\gamma}{\Gamma_t+\gamma-\cos^2(\theta/2)\gamma} w, \\ y &= x, \\ z &= \frac{\cos^2(\theta/2)\gamma}{\Gamma_t+\sin^2(\theta/2)\gamma} x. \end{cases} \tag{13}$$

And $w = \mathcal{F}_\infty$ is the steady state fidelity.

SUPPLEMENTARY NOTE 3: STABILIZATION ROBUSTNESS

We study the stabilization robustness for $|\Psi_-\rangle$ and $|\Phi_-\rangle$ in this section. For other stabilization angles, the discussion is similar. Supplementary Figure 4 shows the rotating frame simulation of steady-state fidelity by sweeping different stabilization parameters. For the $|\Psi_-\rangle$ case, the Hamiltonian used in the simulation is Eq. (1) in the main text, and for the $|\Phi_-\rangle$ case the Hamiltonian is modified accordingly with a different sideband combinations (See Fig. 1(c) in the main text). We study the state fidelity by varying parameters step-by-step towards the ideal case. First, we show that longer qubit dephasing time helps improve steady-state fidelity. In Supplementary Figure 4 (a), we sweep qubit's dephasing time (assuming the same for both qubits) while choosing the following parameters $\{\Omega, \frac{W_1}{2}, \frac{W_2}{2}, \Gamma_1, \Gamma_2\}/2\pi$ in the simulation

$$|\Psi_-\rangle \text{ case }: \{1.4, 0.35, 0.35, 0.30, 0.33\}\text{MHz},$$
$$|\Phi_-\rangle \text{ case }: \{3.0, 0.32, 0.32, 0.30, 0.33\}\text{MHz}.$$

We set the following qubit decoherence time $\{T_1^{q1}, T_1^{q2}\} = \{21, 9\}\mu$s. The steady state fidelities rise above 80% quickly after T_ϕ exceeds 10 µs. The fidelity for odd and even parity bell pairs saturate at 87.3% and 85.0% with the parameters used in the simulation. This demonstrates that steady-state fidelity increases as qubit dephasing time increases.

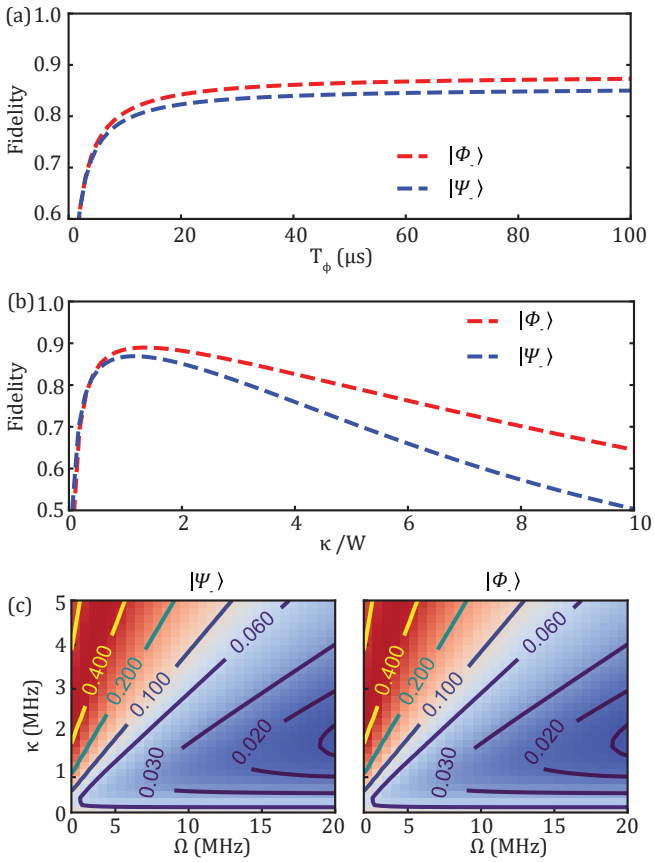

Supplementary Figure 4. Rotating frame simulation of even and odd parity bell states' stabilization fidelity: (a) Sweeping qubit dephasing time. The other simulation parameters are the same as the experiments. (b) Sweeping the ratio between resonator decay rate κ and QR sideband strength W without qubit dephasing. (c) 2D sweep of κ and QQ sideband strength Ω without qubit dephasing, setting $W = \kappa$. Infidelities are shown on the contours.

In Supplementary Figure 4(b), we ignore the qubit dephasing and only sweep resonator decay rate κ. For simplicity, we assume QR sideband rates and resonator decay rate are the same: $W_1 = W_2 = W$ and $\kappa_1 = \kappa_2 = \kappa$. The fidelity peak for both parity pairs appears at $W = \kappa$. This can be understood as the refilling rate Γ_t (Eq. (2) in the main text) achieves the maximum at this point, therefore the steady-state fidelity (Eq. (3) in the main text) is also maximized at this point.

Finally, we choose the maximum refilling rate set $W = \kappa$ in Supplementary Figure 4(c) and sweep both the QQ sidebands rate Ω and resonator decay rate κ. The infidelity of the steady states is shown in contours. Larger Ω and κ suppresses the infidelity efficiently. This indicates

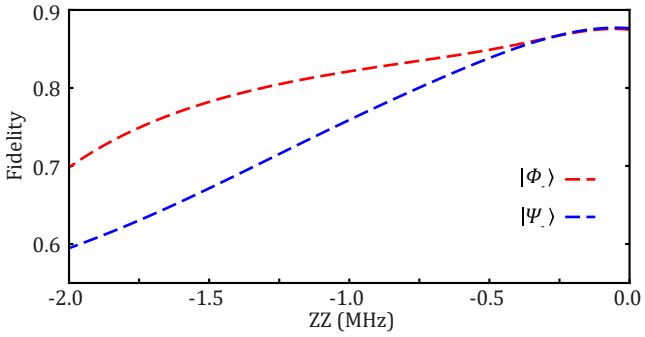

Supplementary Figure 5. Steady state stabilization fidelity under various stray ZZ interactions between qubits. For $|\Psi_-\rangle$ ($|\Phi_-\rangle$), we choose the QQ sideband detunings as $\delta = -ZZ(0)$ for maximum stabilization fidelity.

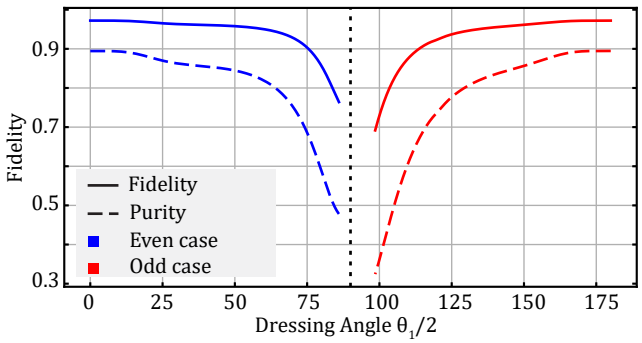

Supplementary Figure 6. Stabilizing a one-dimensional set of entangled states. Blue and red lines represent separately using the QQ blue and QQ red sideband in the rotating frame simulation. Parameter used in the simulation: $\{\Omega, W_1, W_2, \kappa_1, \kappa_2\}/2\pi = \{5.0, 0.5, 0.5, 0.3, 0.33\}$ MHz. Qubit coherence time are $\{T_1, T_\phi\} = \{30, 30\}\mu$s.

that our steady-state fidelity in the experiment is mainly limited by the sideband strengths. By increasing the QQ sidebands rate to above $2\pi \times 10$ MHz, in simulation, it is possible to achieve stabilization fidelity above 98%.

We further investigate the impact of stray ZZ coupling between transmons on stabilization fidelity. This analysis uses the even and odd parity Bell states $|\Phi_-\rangle$ and $|\Psi_-\rangle$ as examples. We choose the following parameters $\{\Omega, \frac{W_1}{2}, \frac{W_2}{2}, \Gamma_1, \Gamma_2\}/2\pi$ in the simulation (the same as the experimental measurements).

$$|\Psi_-\rangle \text{ case :} \{2.0, 0.47, 0.47, 0.33, 0.43\}\text{MHz},$$
$$|\Phi_-\rangle \text{ case :} \{3.0, 0.36, 0.36, 0.33, 0.43\}\text{MHz}.$$

The $Q_1(Q_2)$ coherence used in the simulation are $\{T_1, T_\phi\} = \{25(12), 25(25)\}\mu$s. In the presence of ZZ coupling η, the energy matching requirement $E_A + E_D = E_B + E_C$ is no longer satisfied. The mismatch in energy η reduces the two-step refilling rate $\Gamma_t' = \frac{W^2\cos^2(\theta/2)\kappa}{\kappa^2+W^2\cos^2(\theta/2)+\eta^2}$.

Therefore, stabilization fidelity decreases as the strength of the ZZ coupling increases. However, when the ZZ coupling strength is less than the QR sideband rate W, the refilling rate remains relatively unaffected by changes in η. As shown in Supplementary Figure 5, the stabilization fidelity does not significantly decrease for $ZZ > -0.3$ MHz. Notably, the static ZZ coupling measured in our experiments is -0.261 MHz, which falls within this acceptable range.

SUPPLEMENTARY NOTE 4: OTHER STABILIZATION COMBINATIONS

Here we provide a list of states that can be stabilized with our protocol.

Case 1: Any two-qubit product states.

$$|\psi_{\phi_1,\phi_2}\rangle = (\cos(\phi_1/2)|g\rangle + \sin(\phi_1/2)|e\rangle)\otimes (\cos(\phi_2/2)|g\rangle + \sin(\phi_2/2)|e\rangle). \quad (16)$$

This can be achieved by applying two detuned single qubit rabi drives on both Q_1 and Q_2 with rate $\{A_1, A_2\}$ and detunings $\{\delta_1, \delta_2\}$. The two-qubit rotating frame Hamiltonian becomes

$$H_p = \begin{bmatrix} 0 & A_2/2 & A_1/2 & 0 \\ A_2/2 & \delta_2 & 0 & A_1/2 \\ A_1/2 & 0 & \delta_1 & A_2/2 \\ 0 & A_1/2 & A_2/2 & \delta_1+\delta_2 \end{bmatrix}. \quad (17)$$

It can be easily verified that the four eigenenergies $\{E_A < E_B < E_C < E_D\}$ satisfy the requirements $E_A + E_D = E_B + E_C$. Therefore, the lowest energy eigenstate can be efficiently stabilized by detuning two QR sideband frequencies. This is also a direct extension of the single-qubit stabilization scheme [1] to the two-qubit case.

Case 2: Dressed parity Bell states. The stabilized state set can be described by one continuous variable θ_1

$$|\zeta_{\theta_1}\rangle = \cos(\theta_1/2)|\Psi_-\rangle + \sin(\theta_1/2)|\Phi_-\rangle. \quad (18)$$

In this case, we apply on-resonant QQ blue and single qubit rabi drive on Q_1 with rate Ω and A_1 to dress the stabilized state's parity. The two-qubit Hamiltonian H_b can be written as

$$H_b = \begin{bmatrix} 0 & 0 & A_1/2 & \Omega/2 \\ 0 & 0 & 0 & A_1/2 \\ A_1/2 & 0 & 0 & 0 \\ \Omega/2 & A_1/2 & 0 & 0 \end{bmatrix}. \quad (19)$$

One can verify that the four eigenenergies $E_A < E_B, < E_C < E_D$ of H_b satisfy the requirement $E_A + E_D = E_B + E_C$. By choosing QR sidebands detunings as $E_B - E_A$ and $E_C - E_A$, the eigenstate $|A\rangle = |\zeta_{\theta_1}\rangle$ is stabilized, with the dressing angle being

$$\theta_1 = 2\arctan\left(\frac{2A_1}{\Omega + \sqrt{4A_1^2+\Omega^2}}\right). \quad (20)$$

Similarly, we apply on-resonant QQ red sideband and single qubit rabi drive on Q_1 with rate Ω and A_1. The two-qubit Hamiltonian H_r is

$$H_r = \begin{bmatrix} 0 & 0 & A_1/2 & 0 \\ 0 & 0 & \Omega/2 & A_1/2 \\ A_1/2 & \Omega/2 & 0 & 0 \\ 0 & A_1/2 & 0 & 0 \end{bmatrix}. \tag{21}$$

The dressing angle θ_1 under this case is

$$\theta_1 = \pi - 2\arctan\left(\frac{2A_1}{\Omega + \sqrt{4A_1^2 + \Omega^2}}\right). \tag{22}$$

Steady-state fidelity is calculated through Qutip simulation for both cases, shown in Supplementary Figure 6. By combining different QQ sideband colors, all dressing angles are stabilized with the scheme, except the small band region around $\theta_1 = \pi$ where the effective transition rates provided by QR sidebands are close to 0.

Case 3: Rabi-dressed entangled states. This is a more general case where a two-dimensional set of entangled states is stabilized. We simultaneously apply a single qubit rabi drive on Q_1 with the rate A_1 and detuned QQ blue sideband with rate Ω and detuning δ. The rotating frame Hamiltonian is

$$H_g = \begin{bmatrix} -\delta/2 & 0 & A_1/2 & \Omega/2 \\ 0 & \delta/2 & 0 & A_1/2 \\ A_1/2 & 0 & -\delta/2 & 0 \\ \Omega/2 & A_1/2 & 0 & \delta/2 \end{bmatrix}. \tag{23}$$

The four eigenenergies of the Hamiltonian can also be grouped into two pairs sharing the same sum. By appropriately choosing two QR sideband detunings, the lowest energy eigenstate is stabilized

$$\begin{aligned} |\xi_{\delta,A_1}\rangle =& E_{00}|gg\rangle + E_{01}|ge\rangle + E_{10}|eg\rangle - |ee\rangle, \\ x =& \sqrt{4\delta^2 A_1^2 + 4A_1^2\Omega^2 + \Omega^4}, \\ y =& \sqrt{\delta^2 + 2(2A_1^2 + \Omega^2 + x)}, \\ E_{00} =& \frac{(\delta - y)(\delta^2 + \Omega^2 + x + \delta y)}{2\Omega(2A_1^2 + \Omega^2 + x)}, \\ E_{01} =& \frac{A_1(\delta - y)}{2A_1^2 + \Omega^2 + x}, \\ E_{10} =& -\frac{A_1(\delta^2 + \Omega^2 + x + \delta y)}{\Omega(2A_1^2 + \Omega^2 + x)}. \end{aligned} \tag{24}$$

For brevity, the stabilized state $|\xi_{\delta,A_1}\rangle$ is not normalized. The form of the state is determined by two independent variables $\frac{\delta}{\Omega}$ and $\frac{A_1}{\Omega}$. We sweep these two variables and plot the simulated fidelity and purity in Supplementary Figure 7. This a general map covering all stabilized entangled states in the programmable operation: the vertical cut $\frac{\delta}{\Omega} = 0$ represents the blue line in case 2 Dressed parity Bell states, the horizontal cut $\frac{A_1}{\Omega} = 0$ represents the stabilized states shown in Fig. 1(b) in the main text,

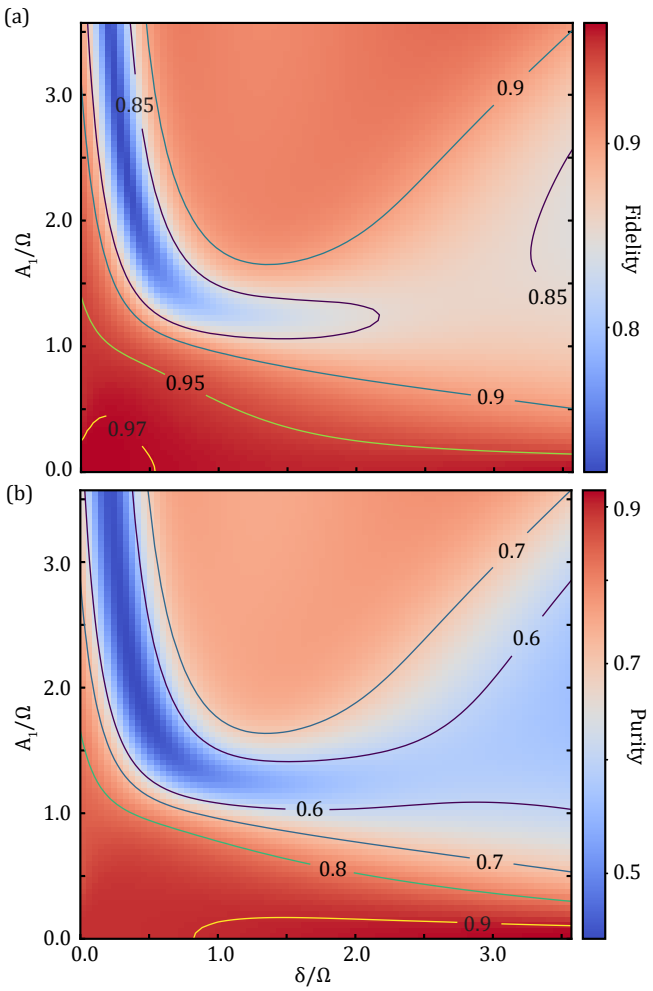

Supplementary Figure 7. Stabilizing a 2D set of entangled states. Steady states' fidelity (a) and purity (b) are simulated in the rotating frame and plotted. $\frac{A_1}{\Omega}$ and $\frac{\delta}{\Omega}$ are separately two free variables that are swept to stabilize different states. Parameter used in the simulation: $\{\Omega, W_1, W_2, \kappa_1, \kappa_2\}/2\pi = \{5.0, 0.5, 0.5, 0.3, 0.33\}$ MHz. Qubit coherence time are$\{T_1, T_\phi\} = \{30, 30\}\mu$s.

and the bottom left point $(\frac{\delta}{\Omega}, \frac{A_1}{\Omega}) = (0, 0)$ is the even parity bell state $|\Psi_-\rangle$. Using a modest sideband rate combination, most of the states on the plot can be stabilized with fidelity over 90%. Correspondingly, changing the QQ sideband color to red can stabilize another 2D set of entangled states which are dual to this case. All possible programmable stabilization operations can be chosen accordingly through the map provided here. States with both $E_{01} > 1$ and $E_{10} > 1$ cannot be stabilized under this case for instance.

SUPPLEMENTARY NOTE 5: EXPANDING STABILIZATION TO MULTIPLE QUBITS' ENTANGLED STATES

In this section, we discuss the possibility of stabilizing N qubits' entangled states. Consider an N-qubit-N-resonator system for simplicity. All interactions for qubits only are included in the Hamiltonian H_Q, and all interactions between each qubit-resonator pair are included in the Hamiltonian H_{QR}. H_{QR} is treated as a perturbation to H_Q. We label the eigenstates and eigenenergies of H_Q as $|i\rangle$, E_i, $i = 1, 2, ..., 2^N$, and $|1\rangle$ is the target stabilized state. We label the photon energy in each resonator as R_j, $j = 1, 2, ..., N$, which are tuned by adding detuned QR sidebands in H_{QR}. R_j can be freely chosen. We further assume that the resonators are sufficiently cold, ensuring that the total excitation number across all resonators does not exceed 1.

We first derive the generalized energy matching requirement for efficient stabilization flow. The goal is to identify all possible energy spectra $\{E_i - E_1\}$ for which our stabilization protocol is effective.

The possible spectra will be constructed iteratively. We will add elements to the energy set S after each step. Once the number of elements in an energy set reaches $2^N - 1$, it qualifies as a possible energy spectrum suitable for efficient stabilization:

Step 0: $S = U = \{R_j\}, E_{j+1} - E_1 = R_j, j = 1, 2, ..., N$.

Next Step: Choose $s_j \in U$, $s_a \in S$, assume $s_j = E_{j+1} - E_1$ and $s_a = E_{a+1} - E_1$, add $s_j + s_a + E_1$ into S.

Stop: When $|S| = 2^N - 1$.

To verify the stabilization of $|1\rangle$, we check if a path to $|1\rangle$ exists for all other states via dissipation and sideband interactions. We label the system's state as $|j\rangle$ without resonator excitations, with qubits in the eigenstate $|j\rangle$. When the k-th resonator is excited, we label the state as $|j, R_k = 1\rangle$:

Step 0: $|j\rangle \leftrightarrow |1, R_{j-1} = 1\rangle \rightarrow |1\rangle$, $j = 2, ..., N + 1$. The first double arrow represents a sideband interaction between two Floquet states of the same energy, and the second arrow represents the resonator dissipation. This shows that any population in $|j\rangle, j = 2, ..., N + 1$ can be transferred to $|1\rangle$.

Next Step: Consider the added energy defined by $s_c = s_a + s_j + E_1 = E_{a+1} + E_{j+1} - E_1 = E_{c+1} - E_1$. Assuming $|a + 1\rangle$ is already part of the stabilization flow. Notice $|c + 1\rangle \leftrightarrow |a + 1, R_j = 1\rangle \rightarrow |a + 1\rangle$ dissipates the population to $|a + 1\rangle$, this confirms that $|c + 1\rangle$ is also integrated into the stabilization flow. When $|S| = 2^N - 1$, all possible eigenstates are included in the flow. Therefore, $|1\rangle$ is stabilized.

For instance, when N=2, one can verify that there are 2 classes of the energy spectrum for efficient stabilization, and the first class is achieved in our experiment:

$S = \{E_2 - E_1, E_3 - E_1, E_2 + E_3 - E_1\}$, and

$S = \{E_2 - E_1, E_3 - E_1, 2E_2 - E_1\}$.

For N=1, there is no requirement for the energy spectrum. Therefore, all product states can be stabilized by simply detuning the resonator photon's energy.

The challenge lies in constructing H_Q based on a target state $|1\rangle$ to stabilize. H_Q must not only have $|1\rangle$ as its ground state, but its energy spectrum must also meet the previously imposed requirements. While experimental demonstrations of stabilization are realized for $N = 1, 2$, the difficulty increases dramatically as the number of eigenstates increases exponentially with N, and for $N = 3$, even finding a possible H_Q is not obvious. Providing a detailed, constructive example remains an objective for future work.

SUPPLEMENTARY NOTE 6: QR SIDEBAND COLORS AND DETUNINGS

Changing sideband colors and detuning frequency signs stabilize different states. This is important for stabilizing $|\Psi_\theta\rangle$ and $|\Phi_\theta\rangle$: at certain blending angles the steady state fidelity is low because of the low effective refilling rate Γ_t (See Eq. (2) in the main text).

As an explicit example, we consider the $|\Psi_\theta\rangle$ stabilization case. Instead of using two QR blue sidebands, we use two QR red sidebands with the same detuning and sideband rate. The rotating frame Hamiltonian now becomes

$$\begin{aligned} H_{\text{color}} =& \frac{\Omega}{2}\left(a_{q1}a_{q2} + h.c.\right) + \delta a_{q1}^\dagger a_{q1} \\ &+ \frac{W_1}{2}\left(a_{q1}^\dagger a_{r1} + h.c.\right) + \frac{W_2}{2}\left(a_{q2}^\dagger a_{r2} + h.c.\right) \\ &+ \frac{\Delta + \delta}{2} a_{r1}^\dagger a_{r1} + \frac{\Delta - \delta}{2} a_{r2}^\dagger a_{r2}. \end{aligned} \tag{25}$$

Supplementary Figure 8 (a) shows the level diagram, where the QR red sidebands now connect $|ge00\rangle$ to $|\Psi_\theta 01\rangle$, which is different from the QR blue sidebands case where $|ge00\rangle$ and $|\Psi_\theta 10\rangle$ are connected. The two-step refilling rate Γ_{tc} for $|ge00\rangle \rightarrow |\Psi_\theta 00\rangle$ is

$$\Gamma_{tc} = \frac{W^2 \sin^2(\theta/2)\,\kappa}{\kappa^2 + W^2 \sin^2(\theta/2)}. \tag{26}$$

The other three two-step transitions $|eg00\rangle \rightarrow |\Psi_\theta 00\rangle$, $|\Psi_{\theta-\pi} 00\rangle \rightarrow |ge00\rangle$, and $|\Psi_{\theta-\pi} 00\rangle \rightarrow |eg00\rangle$ have the same refilling rate. Therefore, the steady-state fidelity for $|\Psi_\theta\rangle$ is

$$\mathcal{F}_\infty = \left(\frac{\Gamma_t + \gamma\cos^2(\theta/2)}{\Gamma_t + \gamma}\right)^2. \tag{27}$$

One can thus choosing the QR sideband color for higher F_∞. When the F_∞ drops significantly near $\theta = \pi$ for Φ_θ stabilization case, one can flip the QR sideband color for better performance.

We can also keep the same QR sideband color while choosing opposite QR sideband detunings. The Hamil-

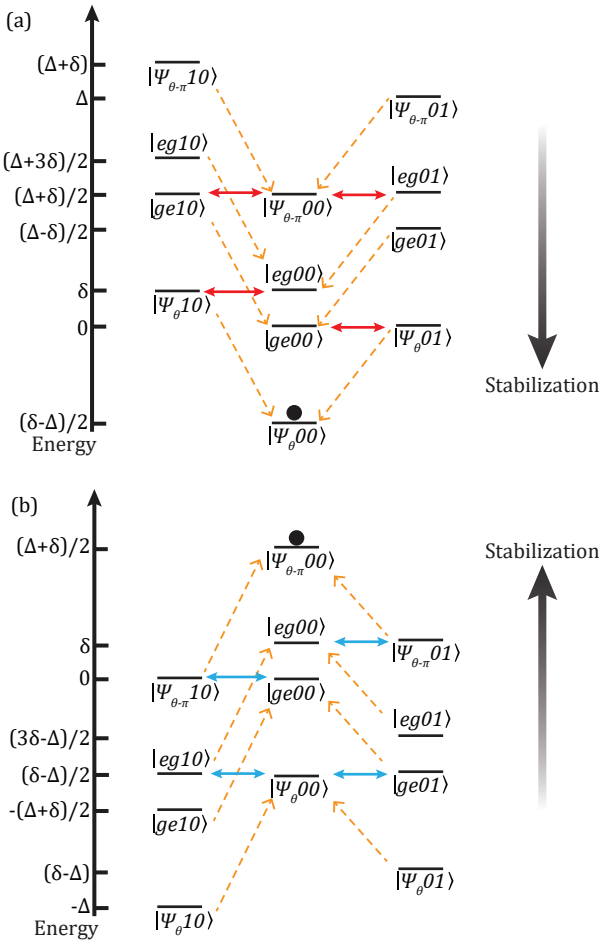

Supplementary Figure 8. (a) Use both QR red sidebands to stabilize $|\Psi_\theta\rangle$. (b) Use opposite QR blue sideband detunings to stabilize $|\Psi_{\theta-\pi}\rangle$. The QQ sideband rates and detunings are separate Ω and δ, and the QR sideband is detuned in frequency by $\frac{\Delta+\delta}{2}$, $\frac{\Delta-\delta}{2}$ in (a) and $-\frac{\Delta+\delta}{2}$, $-\frac{\Delta-\delta}{2}$ in (b). Here $\Delta=\sqrt{\Omega^2+\delta^2}$.

tonian becomes

$$\begin{aligned} H_{\text{opp}} =& \frac{\Omega}{2}\left(a_{q1}a_{q2}+h.c.\right)+\delta a_{q1}^{\dagger}a_{q1} \\ &+\frac{W_1}{2}\left(a_{q1}^{\dagger}a_{r1}+h.c.\right)+\frac{W_2}{2}\left(a_{q2}^{\dagger}a_{r2}+h.c.\right) \\ &-\frac{\Delta+\delta}{2}a_{r1}^{\dagger}a_{r1}-\frac{\Delta-\delta}{2}a_{r2}^{\dagger}a_{r2}. \end{aligned} \tag{28}$$

The level diagram is shown in Supplementary Figure 8 (b). All population flows to $|\Psi_{\theta-\pi}\rangle$, with the same refilling rate (Eq. (2) in the main text) and steady-state fidelity (Eq. (3) in the main text) as the $|\Psi_\theta\rangle$ case.

SUPPLEMENTARY NOTE 7: MEASUREMENT SETUP

Supplementary Figure 9 illustrates the measurement setup used in the experiment. Both single qubit, QR sidebands, and QQ sidebands signals are generated with a 4-channel AWG (Keysight M8195 65 Gsa/s, 16 Gsa/s per channel) to maintain phase-locking. DC flux bias for the coupler and two Josephson Parametric Amplifiers (JPAa) are generated with three current sources (Yokogawa GS200). The bandpass filters on both charge lines are chosen such that the stop band covers both readout and qubits' frequencies. The flux drive is delivered using three separate coaxial cables for DC bias, red sideband and blue sideband frequencies. The RF lines are merged using a combiner which is then added to the DC bias using a bias tee. The Stepped impedance Purcell filter (SIPF) inserted in the flux line is a home-made filter with a stop band between 2 GHz and 5.5 GHz blocking any qubit and resonator signals. Each transmitted signal is first amplified by a JPA with a +15 dB gain, followed by a HEMT amplifier and three room-temperature amplifiers. The final signal is pre-amplified after demodulation and digitized with an Alazar ATS 9870 (1GSa/s) card.

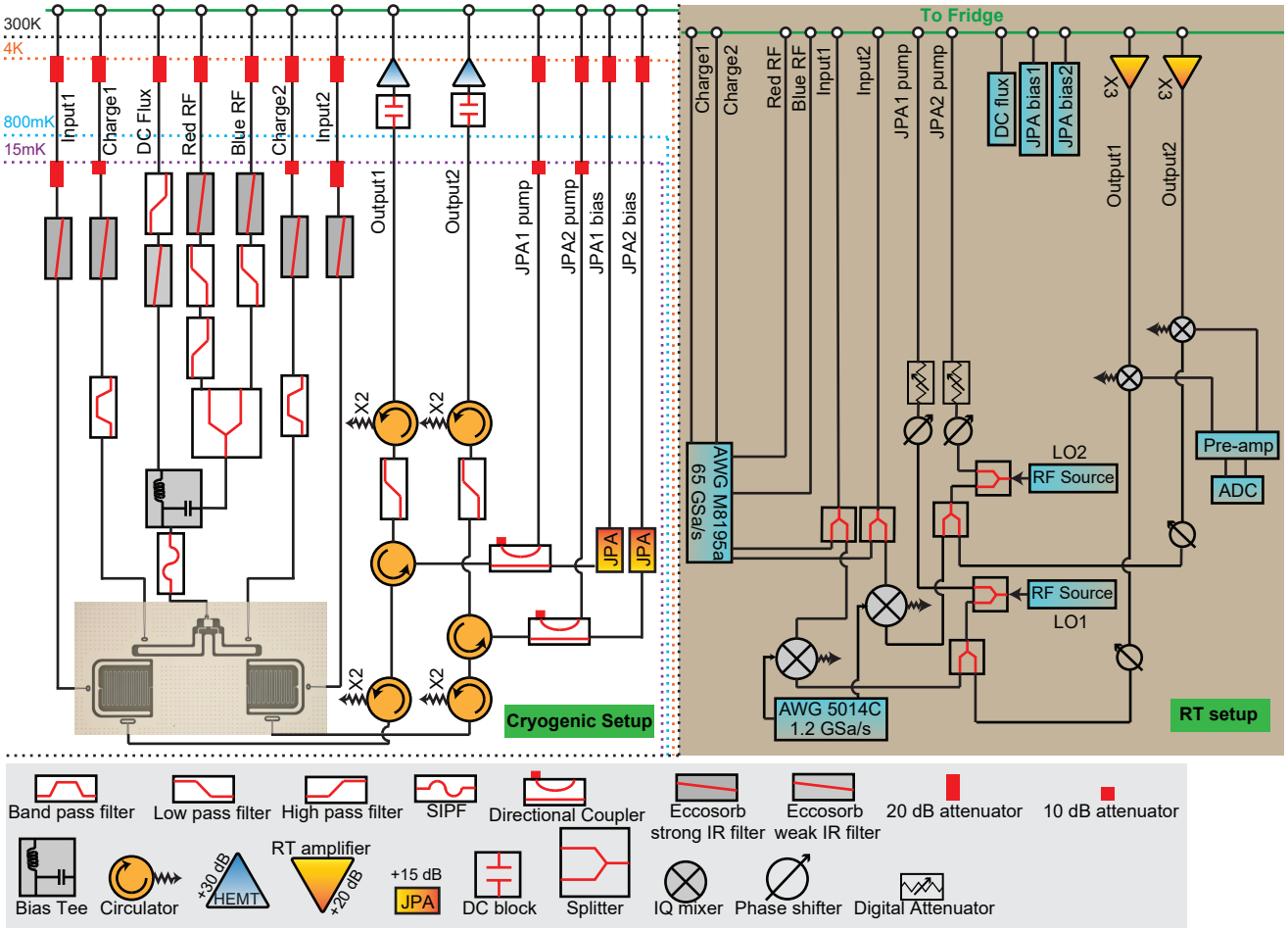

Supplementary Figure 9. Detailed measurement setup.

[1] Y. Lu, S. Chakram, N. Leung, N. Earnest, R. K. Naik, Z. Huang, P. Groszkowski, E. Kapit, J. Koch, and D. I. Schuster, Universal stabilization of a parametrically coupled qubit, Phys. Rev. Lett. **119**, 150502 (2017).

[2] Z. Li, T. Roy, D. Rodríguez Pérez, K.-H. Lee, E. Kapit, and D. I. Schuster, Autonomous error correction of a single logical qubit using two transmons, Nature Communications **15**, 1681 (2024).

[3] A. Wallraff, D. I. Schuster, A. Blais, J. M. Gambetta, J. Schreier, L. Frunzio, M. H. Devoret, S. M. Girvin, and R. J. Schoelkopf, Sideband transitions and two-tone spectroscopy of a superconducting qubit strongly coupled to an on-chip cavity, Phys. Rev. Lett. **99**, 050501 (2007).